A Fully Integrated Broadband Sub-mmWave Chip-to-Chip Interconnect

Jack W. Holloway, *Student Member, IEEE*, Luciano Boglione, *Senior Member, IEEE*, Timothy M. Hancock, *Senior Member, IEEE*, and Ruonan Han, *Member, IEEE*

***Abstract*— A new type of broadband link enabling extremely high-speed chip-to-chip communication is presented. The link is composed of fully integrated sub-mmWave on-chip traveling wave power couplers and a low-cost planar dielectric waveguide. This structure is based on a differentially driven half-mode substrate integrated waveguide supporting the first higher order hybrid microstrip mode. The cross-sectional width of the coupler structure is tapered in the direction of wave propagation to increase the coupling efficiency and maintain a large coupling bandwidth while minimizing its on-die size. A rectangular dielectric waveguide, constructed from Rogers Corporation R3006 material, is codesigned with the on-chip coupler structure to minimize coupling loss. The coupling structure achieves an average insertion loss of 4.8 dB from 220 to 270 GHz, with end-to-end link measurements presented. This system provides a packaging-friendly, cost effective, and high performance planar integration solution for ultrabroadband chip-to-chip communication utilizing millimeter waves.**

***Index Terms*— Chip-to-chip, dielectric waveguide, leaky wave antenna (LWA), power coupler, substrate integrated waveguide (SIW), sub-mmWave, traveling wave.**

I. Introduction

TRADITIONAL interchip interconnect technologies, when deployed for terascale data storage and computing, face severe problems in transfer speed and energy consumption. The excessive ohmic loss and dispersion associated with copper interconnects in high performance electronic systems have led to a number of efforts focusing on characterization of the physical interconnects, high-speed drivers, and channel equalization [1]–[3] in an attempt to mitigate these challenges. In addition, solutions to the board-level (1–10 cm link length) and back plane-level (10–100 cm link length) interconnects have garnered much attention around electro-optical solutions. These solutions suffer from integration issues surrounding laser sources, waveguides, and photonic devices with traditional silicon systems [3]–[8], as well as electrical-optical/optical-electric conversion and waveguide-chip interfacing issues associated with coupling power on- and off-chip [3], [8]–[12].

A number of efforts have focused on all-electronic solutions to the short-range chip-to-chip communication problem, involving coupling a modulated mmWave or sub-mmWave carrier into a dielectric waveguide [3], [13]–[22]—so-called "radio over fiber" schemes. These concepts attempt to harness the wider available bandwidths at these higher frequencies, and require on- and off-chip apertures to radiate into polymer or silicon waveguides. Compared to the work presented in this paper, previously demonstrated schemes use lower carrier frequencies, leading to lower bandwidth and I/O density. A number of these works are based on off-chip components, which introduce integration challenges and do not readily lend themselves to higher frequency operation.

Techniques utilizing off-chip radiators [3], [13]–[15], [19], illustrated in Fig. 1(a), aside from increasing system integration complexity, inherently trade the original bandwidth-distance constraint of copper interconnects in driving an off-chip coupler. This effect manifests itself as a decrease in coupling efficiency. In [13], a dual band coupler, utilizing mode orthogonality, was demonstrated with a bandwidth of 35 GHz and coupling loss of 5 dB. A number of efforts have utilized die-to-package bond wires or patch antennas as radiators, coupling energy into plastic tube waveguides [16], [17], [22]. In [16], a coupler was demonstrated with a bandwidth of 6 GHz and a coupling loss of 6 dB utilizing air core plastic tube waveguides. This approach (and those used in [17] and [17]) is illustrated in Fig. 1(b). It presents a number of integration challenges in packaging, especially when high-density I/O integration is needed. Lastly, work has been done on utilizing integrated on-chip antennas to couple modulated carriers into waveguides [3], [18], as shown in Fig 1(c). In [3], a coupler with a bandwidth of 8 GHz was implemented using a micromachined silicon waveguide, exhibiting a coupling loss of 5.8 dB. While these efforts address the need for an on-chip coupler, they suffer from the well-known bandwidth-radiation efficiency tradeoffs associated with on-chip resonant antennas [23], [24]. This approach

Manuscript received July 25, 2016; revised November 24, 2016 and January 5, 2017; accepted January 6, 2017. Date of publication February 20, 2017; date of current version June 29, 2017. This work was supported in part by the Office of Naval Research under Award N00014-15-1-2429 and Award N00014-16-1-2322, in part by the MIT Lincoln Laboratory Military Fellows Program, in part by the MIT Center for Integrated Circuits and Systems, and in part by Analog Device Inc.

J. W. Holloway is with the Office of Naval Research, Arlington, VA 22217 USA, with the Massachusetts Institute of Technology, Cambridge, MA 02139 USA, and also with the Naval Research Laboratory, Washington, DC 20375 USA (e-mail: holloway@mit.edu).

L. Boglione is with the Electromagnetic Science and Technology Division, Code 6850, Naval Research Laboratory, Washington, DC 20375 USA (e-mail: luciano.boglione@nrl.navy.mil).

T. M. Hancock is with the DARPA Microsystems Technology Office, Arlington, VA 22203 USA, and also with the RF Technology Group, Lincoln Laboratory, Massachusetts Institute of Technology, Lexington, MA 02421 USA (e-mail: hancockt@ll.mit.edu).

R. Han is with the Department of Electrical Engineering and Computer Science, Massachusetts Institute of Technology, Cambridge, MA 02139 USA (e-mail: ruonan@mit.edu).

Color versions of one or more of the figures in this paper are available online at http://ieeexplore.ieee.org.

Digital Object Identifier 10.1109/TMTT.2017.2660491

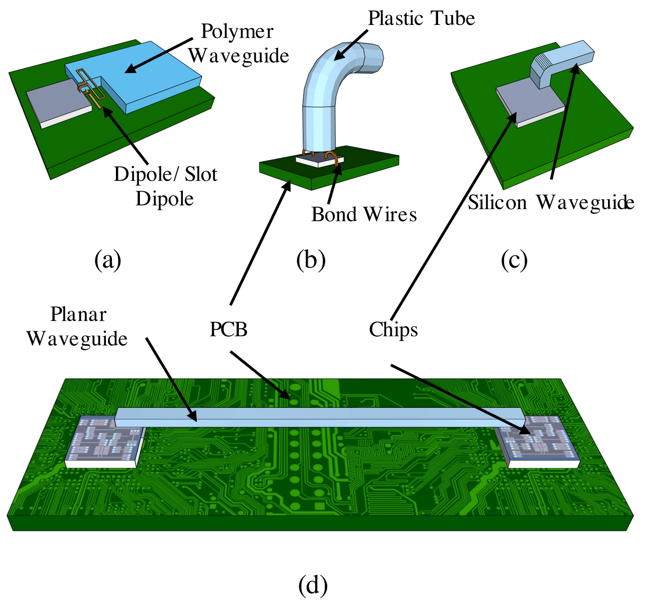

Fig. 1. Illustration of the 3-D integration challenges surrounding chip-to-chip links. (a) Off-chip planar waveguide, dipole/slot dipole couplers from [13]–[15] (the waveguide cutaway is included to illustrate both of the off-chip couplers). (b) Bond wire couplers and plastic tube waveguide in [16], [17]. (c) Micromachined silicon waveguide sitting at a 90° angle above an on-chip patch antenna coupler described in [3] and [18]. (d) Fully planar chip-waveguide interface presented in this paper.

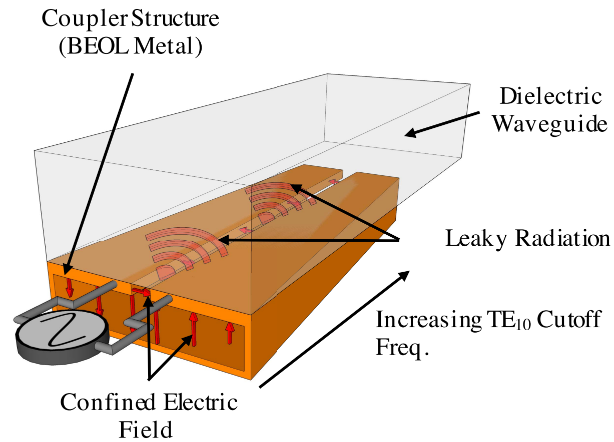

Fig. 2. Conceptual illustration of a tapered HM-SIW as presented in this paper.

also requires the waveguide interface itself to be normal to the radiator surface to maximize the coupling efficiency.

In this paper, we propose a link based on the 220–325 GHz dielectric waveguide and a new class of integrated traveling wave coupler. This coupler is based on a differentially driven half-mode substrate integrated waveguide (HM-SIW) topology. This structure is compatible with existing commercial integrated circuit (IC) processes and requires no wafer postprocessing. This coupler lends itself to straightforward planar integration with a simple rectangular dielectric waveguide. The overall system-level integration concept is illustrated in Fig. 1(d). The sub-mmWave frequency range provides much higher bandwidth and data rate compared to mmWave approaches. In addition, the smaller wavelengths in the sub-mmWave regime, compared to mmWave frequency ranges, provide smaller waveguide sizes and smaller guide-to-guide pitches, further increasing the density of high-bandwidth links.

The rapid progress of sub-mmWave and THz signal generation and detection in silicon processes has also spurred interest in modulated sub-mmWave and THz waves for wireline communication. Power generation at these frequencies in silicon normally relies on the use of nonlinearities to produce harmonics, from which the appropriate frequency component is extracted [25]. In [26], a SiGe-based THz harmonic oscillator is demonstrated with a dc-to-THz conversion efficiency of 2.4%. With increasing silicon device cutoff frequencies, the use of fundamental-mode power generation is an attractive potential, with subsequent improvements in dc-to-THz conversion efficiency. Additionally, receivers in silicon have been demonstrated with sensitivity as low as 29 pW/$\sqrt{\text{Hz}}$ [27]. Assuming a nominal detector noise equivalent power (NEP) comparable to that demonstrated in [27], an additive white Gaussian noise (AWGN) channel, available bandwidth of 50 GHz, channel and coupler loss of approximately 20 dB, and dc-to-THz conversion efficiencies reported in the literature we expect a theoretical link efficiency better than 1 pJ/b (the Appendix). The use of coherent detection may further improve the efficiency of such a link [28]. These link efficiency figures make this technology attractive for terascale links with high-density integration.

One of the key enabling technologies for such a THz link, a power coupler, is conceptually illustrated in Fig. 2. This structure, fully implemented in a silicon chip, requires neither wafer postprocessing nor off-chip radiators, and presents a low-cost and readily integrated solution for high-bandwidth short range chip-to-chip communication. The proposed structure is measured with more than 50 GHz of bandwidth, a coupling loss of 4.8 dB, and flat dispersion across the frequency band of 220–270 GHz. To the best of the authors' knowledge, these performance metrics represent the best reported to date.

The structure of this paper is as follows. Section II covers the development of analytical models to approximate the electromagnetic behavior of the coupler structure, as well as the dielectric waveguide. Section III describes the parametric optimization, design, and implementation of the on-chip components, dielectric waveguide, and test fixtures. Section IV discusses the measurement setup and procedures, the measurement results of the insertion loss associated with the coupler and various lengths of dielectric waveguide, as well as a comparison with data available in the literature. Section V concludes this paper with a summary of achievements.

II. On-Chip Apertures

At sub-mmWave and THz frequencies, on-chip resonant radiators atop bulk silicon tradeoff bandwidth for radiation efficiency [23]. In the case of an unshielded radiator, a dipole or unbacked slot radiator, for example, the majority of the radiated energy preferentially couples into the bulk silicon. A silicon lens can be used to more efficiently radiate this power into free space [29] from the rear of the chip, but in doing so, one sacrifices integration cost and complexity. Backing a radiator with a ground plane may significantly improve the radiator efficiency. However, given the back-end-of-line (BEOL) interconnects available in modern silicon IC processes, the proximity of the ground plane and the radiator produces a high Q resonance dramatically lowering the radiation bandwidth [30].

A number of techniques can be used to increase on-chip antenna bandwidth. In [31], parasitic reflectors were added to increase both the bandwidth and efficiency, as well as the directivity of the radiator. In [32] and [33], extra resonances are designed into the aperture to extend antenna bandwidth. However, the antenna still radiates in the broad side which is incompatible with a planar coupling solution. Leaky wave antennas (LWAs) have been used for efficient on-chip broadband radiation [30], and generally provide excellent directivity, as well as excellent beamwidth for use in a quasi-optical coupling scheme. These structures, however, require significant aperture lengths (on the order of several wavelengths) to maintain radiation efficiency [30], [34]–[37]. This issue is of particular concern as related to on-chip integration. Any step taken to maintain or increase bandwidth and radiation efficiency, and decrease required physical size would make LWAs more attractive for on-chip integration. This paper makes use of a modified LWA structure in which the coupler cross section is tapered to capitalize on the traveling wave structure's inherent bandwidth while decreasing the required structure length.

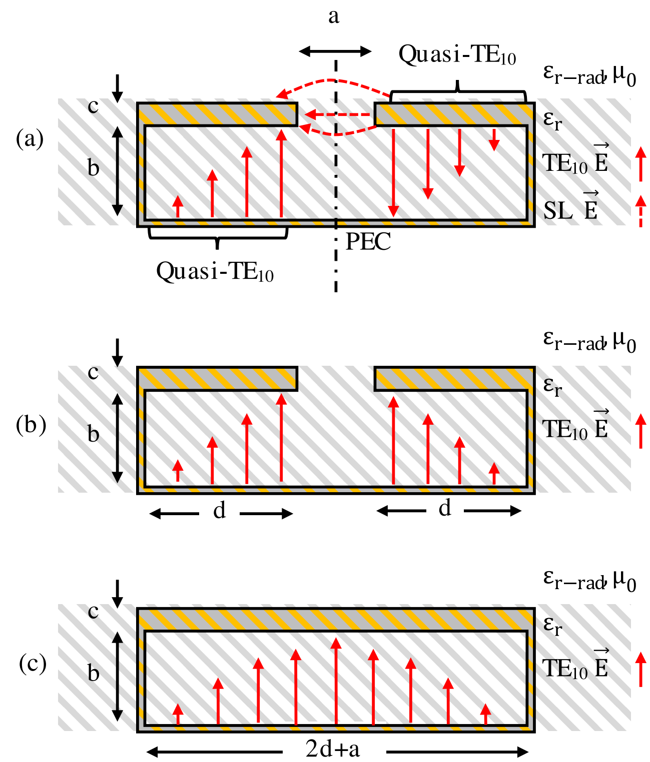

Fig. 3. Three structures with the same cross section. (a) Presented structure supporting the odd EH_1. (b) Presented structure supporting the even EH_1 mode. (c) TE_{10} mode in the same size structure as the gap a goes to zero width. The solid lines correspond to the those portions of the mode that resembles a portion of a standard rectangular waveguide TE mode, while the dashed lines in the odd EH_1 mode resemble that portion of the field resembling a slot line mode.

A. Differential HM-SIW Leaky Wave Coupler

Single-sided HM-SIW antennas are traveling wave radiators that support the first microstrip higher order mode (generally referred to as the EH_1 mode). Constant-cross-sectional variants have been integrated on chip, and their single- and differentially driven [Fig. 3(b)] variants have been demonstrated in arrays [30], [38], [39]. In [38], it was shown that the frequency at which a mode is said to be in the leaky wave region, defined as

$$\alpha < \beta < k_0\sqrt{\epsilon_{r-\mathrm{rad}}} \tag{1}$$

can be decreased if the structure is excited by the odd EH_1 mode. k_0 is the free space wavenumber. The longitudinal wave number is defined as

$$k_z = \beta - j\alpha \tag{2}$$

and the dielectric constant of the material where the leaky wave power radiates is denoted by $\epsilon_{r-\mathrm{rad}}$ (Fig. 3). Here β is the propagation constant and α is the corresponding attenuation constant of a time-harmonic mode.

Consider a constant cross-sectional structure illustrated in Fig. 3(a)–(c). The inner dimension of the full HM-SIW width is denoted by $2d+a$, with the inner height dimension b, the slot width a, and the top conductor thickness c. The HM-SIW coupler is filled with a material with dielectric constant ϵ_r. The entire structure couples to a infinite half-space with dielectric constant $\epsilon_{r-\mathrm{rad}}$.

This structure supports both even and odd EH_1 modes [Fig. 3(a) and (b)], respectively. As was shown in [38], when supporting the odd EH_1 mode [as shown by the solid and dashed red arrows in Fig. 3(a)], the frequency at which leaky-wave behavior begins for a given structure width is decreased over that of a half-mode LWA or the same structure excited by the even EH_1 mode. In addition, using the odd EH_1 mode increases the power radiated due to leaky radiation (described by the attenuate constant α) at a given frequency over the even EH_1 mode or a traditional half-mode LWA. By utilizing the odd EH_1 mode, for a given cross section, the amount of energy coupled into a space-leaky mode can be enhanced and the overall required radiator length decreased while maintaining coupling efficiency compared with a structure excited by the even EH_1 mode or a half-mode LWA supporting a TE_{10} mode.

When excited with the odd EH_1 mode, a portion of the electric field contained within the structure and far from the central slot resembles half of a TE_{10} rectangular waveguide mode [Fig. 3(c)]. In the following discussion, we will refer to this portion of the mode as the quasi-TE_{10} portion, and this portion of the field is denoted by the solid red lines in Fig. 3(a). Near the center slot, the increased electric field strength across the gap causes the electric field lines from the top conductor near the gap to terminate, not vertically

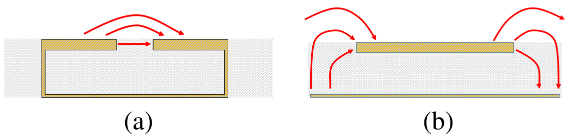

Fig. 4. Comparison of the near-field electric field lines around (a) presented coupler structure supporting the odd EH_1 mode and (b) patch antenna.

onto the bottom conductor, but rather on the top conductor on the opposite side of the gap. These fields are similar to a conductor-backed slot-line mode. This portion of the mode is denoted by the dashed electric field lines.

It should be noted that, for a given guide width $2d + a$, which is approximated by $2d$, at frequencies above

$$f_{\mathrm{TE}} \approx \frac{c_0\sqrt{\epsilon_r}}{4d} \tag{3}$$

where c_0 is the free-space speed of light, the energy in the quasi-TE_{10} field is well-confined in those rectangular waveguide regimes on the structure to the left and right of the center slot. As the wavelength of the supported mode is increased, each rectangular guide section of length d can no longer fully support a quarter wave, and some portion of this energy is coupled into the electric field supported between the center slot and the bottom conductor. This portion of the mode is shown by the slot-line fields denoted by the dashed field lines in Fig. 3(a). Once this energy has been coupled into this regime, it will radiate away from the structure in a space leaky mode if the mode's propagation constant satisfies (1). In the slot and near field, this structure produces an electric field in which the major component is aligned horizontally [Fig. 4(a)], which is matched with the desired horizontally polarized mode in the dielectric waveguide (Fig. 8). The similarity between the desired waveguide mode and coupler radiative modes aides in energy coupling. This is in contrast with the field distribution created by a traditional patch antenna [Fig. 4(b)], as was used in [3] and [18]. The fringe fields at the edge of a patch form horizontally polarized electric fields in the far field, but the near-field modes have much more structure. Traditional patch antennas exhibit larger near-field electric field intensity at the edge with smaller field intensity in the center of the patch. The dissimilarity, in the near field, of this mode and the desired waveguide mode does not encourage energy coupling from the radiative mode into the waveguide mode.

By decreasing the structure width, $2d$, longitudinally (as illustrated in Fig. 2), such a structure produces regions in which energy in a previously propagating quasi-TE_{10} portion of the mode impinges on a narrower cross section where that energy couples into the field supported across the center gap. By virtue of the differential excitation (the odd EH_1 mode), this same structure facilitates the lower frequency onset of space-leakage, as defined in (1), and simultaneously increases the rate of leakage α over the leaky regime [38]. In this way, this structure is able to radiate with the same efficiency while requiring less length.

If implemented on chip, this structure provides a number of advantages over traditional on-chip antennas. It is noteworthy that the proposed coupler structure provides the following three advantages over the prior on-chip designs.

1) Its enclosed nature provides mode confinement away from the bulk silicon, thus decreasing unwanted energy coupling into the substrate.
2) The proposed structure is a traveling wave structure leading to a wider bandwidth than in resonant structures.
3) The coupler near-field mode is structurally similar to the desired mode of the dielectric waveguide, improving coupling efficiency.

B. Analytical Transverse Resonance Model

Structures similar to that presented in Fig. 3(b) have been studied using modal analysis in [40] and [41], but these analyses assumed a zero-thickness top conductor. However, the IC process in which our structure is implemented makes use of a thick top metal of thickness c. The conductor-backed slot-line and its odd hybrid mode behavior have also been extensively modeled, utilizing both modal analysis and circuit approximations [42]. This analysis does not support modes constrained laterally in the bottom portion of the structure. The operation of the proposed structure relies on the vertical SIW walls to contain energy that might otherwise be dissipated into bulk silicon surface waves. In a comparison with full-wave analysis, both of the aforementioned analyses were found to deviate significantly.

An analytical model of the relationship of the odd EH_1 mode longitudinal propagation constant, k_z, as a function of guide dimensions, is desired. Such a model provides insight into the space leaky wave behavior, or the propagation constant β to be specific, as the cross section of the structure is modified. We first consider a uniform cross-sectional HM-SIW leaky-wave coupler [Fig. 3(a) and (b)]. We assume the conductors (physically realized by aluminum metallization and arrays of tungsten vias) are perfect electric conductors (PECs). Next, we note that the electric field distribution of the odd EH_1 mode [Fig. 3(a)] is differentially symmetric, and thus its transverse equivalent network can be represented by a half structure utilizing a PEC boundary condition [Fig. 5(a)].

The geometry in Fig. 5(a), using an approach modified from [37] and [43] for the fields in and around the gap, can be analyzed by a closed-form transverse resonance expression. The resonance condition plane T, denoted by the dashed horizontal line in Fig. 5(b), provides a convenient reference with which to categorize the energy stored in various portions of the fringe fields near the center gap. Modifications to lumped element approximations for the energy storage and coupling mechanisms for an air filled rectangular guide based on E-plane tee junction models from [37] and [43] are reproduced here with appropriate modifications for different dielectric constants and differential energy storage not accounted for in the original analysis.

The susceptances $2B_L$ and B_a account for the stored energy in the main guide (below the resonance plane T) underneath the slot [Fig. 5(b)]. In the following analysis, each lumped element is normalized by the transverse guide characteristic admittance Y_0 of the rectangular waveguide portions of the structure in Fig. 3(b). Enhancing the analysis in [37] to account for dielectric fill and odd-mode symmetry, we write

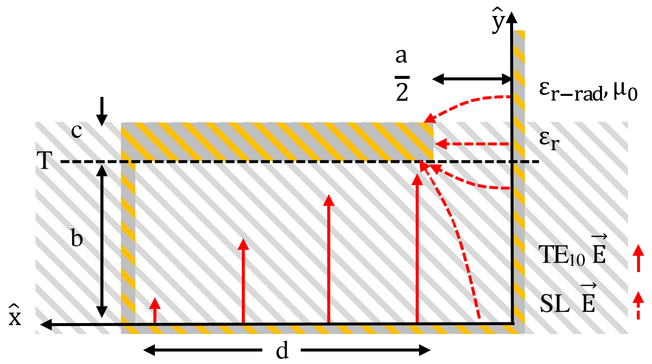

(a)

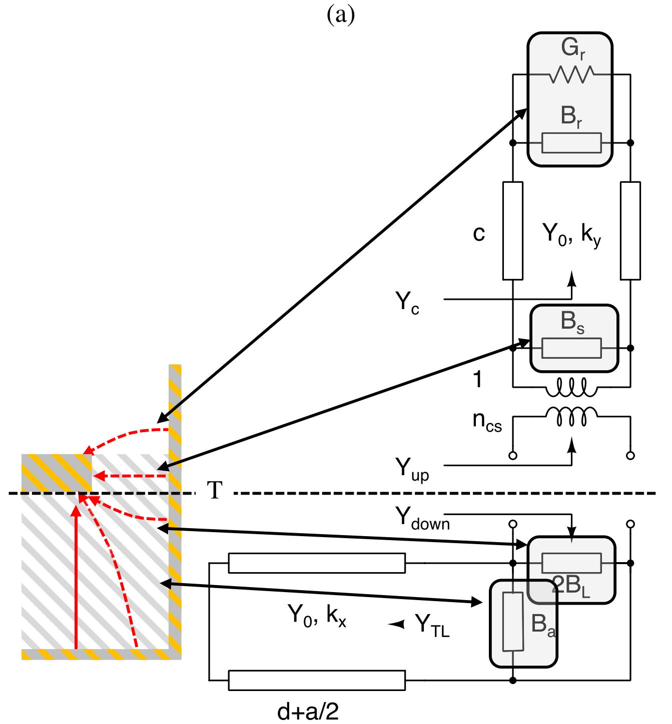

(b)

Fig. 5. (a) HM-SIW EH_1 equivalent half structure. (b) Equivalent transverse resonance circuit model.

the susceptances for the slot-line-like fields as

$$\frac{B_L}{Y_0} = \frac{\epsilon_r}{n_c^2}\left(\frac{k_x b}{\pi}\right)\left[\ln\left(1.43\frac{b}{a}\right) + \frac{1}{2}\left(\frac{k_x b}{\pi}\right)^2\right.$$
$$\left.\cdots + \frac{\pi}{32}\frac{a}{b}\left(k_x\frac{a}{2}\right) J_0^2\left(k_x\frac{a}{2}\right)\right] \tag{4}$$

$$\frac{B_a}{Y_0} = -\frac{\pi}{16}\frac{a}{b}\left(k_x\frac{a}{2}\right) J_0^2\left(k_x\frac{a}{2}\right) \tag{5}$$

where J_0 is the Bessel function of the first kind, and

$$n_c = \frac{\sin\left(k_x\frac{a}{2}\right)}{k_x\frac{a}{2}}. \tag{6}$$

These expressions arise from the analysis of E-plane tee junctions and the integration of the electric modal functions across the gap above and below the resonance plane T when excited by a symmetric magnetic field [37], [43], [44].

The admittance looking into the left side of the shorted transmission line (Fig. 5) from the right, representing the half-width guide along the x-axis of length $d + (a/2)$, can be written as

$$\frac{Y_{TL}}{Y_0} = -j\cot\left(k_x\left(d + \frac{a}{2}\right)\right). \tag{7}$$

The wavenumber k_x, as driven by structure geometry, is used as the parameter to ultimately tune the leaky-wave behavior of the structure.

Above the resonance plane T, we assume that the gap is narrow enough such that only a transverse electric field is supported across the gap. In the gap between the top conductors, from T to the $\epsilon_r - \epsilon_{r-\mathrm{rad}}$ dielectric interface, a horizontally polarized TE_{10} mode (that is $E_x \neq 0$, $E_y = E_z = 0$), is supported in the vertical $\hat{y}$ direction. The equivalent susceptances of the energy stores in the field directly above T are written as

$$\frac{B_s}{Y_0} = \frac{4b}{\lambda_g}\ln\csc\frac{\pi a}{2b} \tag{8}$$

where the guide wavelength is

$$\lambda_g = \frac{\lambda_0}{\sqrt{\epsilon_r - \left(\frac{\lambda_0}{4d}\right)^2}}. \tag{9}$$

The coupling coefficient, modeled by the transformer in Fig. 5(b) with a turns ratio of

$$n_{cs} = n_c\sqrt{\frac{a}{b}} \tag{10}$$

accounts for the difference in the modal voltages in the horizontal portion of the structures and those in the gap [36]. The short section of vertical parallel plate, of length c along $\hat{y}$, seen from reference plane T and up can be represented as a short transmission line of length c. We can write the admittance looking into this transmission line as

$$\frac{Y_c}{Y_0} = \frac{\frac{Y_r}{Y_0} + j\tan k_y c}{1 + j\frac{Y_r}{Y_0}\tan k_y c}. \tag{11}$$

The equivalent radiation admittance from a rectangular waveguide into a dielectric half-space is

$$\frac{Y_r}{Y_0} = \frac{G_r + jB_r}{Y_0} = \frac{\sinh\left(\frac{k_y a}{2}\right) + j\sqrt{\epsilon_r}\sin A}{\cosh\left(\frac{k_y a}{2}\right) + \cos A} \tag{12}$$

for

$$A = \frac{k_y a}{\pi}\ln\left(\frac{e}{\gamma}\frac{4\pi}{k_y a}\right)$$
$$-2\sum_{n=1}^{\infty}\left[\sin^{-1}\left(\frac{k_y a}{2\pi}\frac{1}{n}\right) - \left(\frac{k_y a}{2\pi}\frac{1}{n}\right)\right] \tag{13}$$

where $\gamma \approx 1.781$ and Napier's constant, e, is 2.718 [44]. In addition, we have assumed a single transverse electric mode above T in Fig. 5(a) and single TE mode operation in the horizontal portion of the structure to the left of the gap in Fig. 5(a). As this entire region is filled with the same

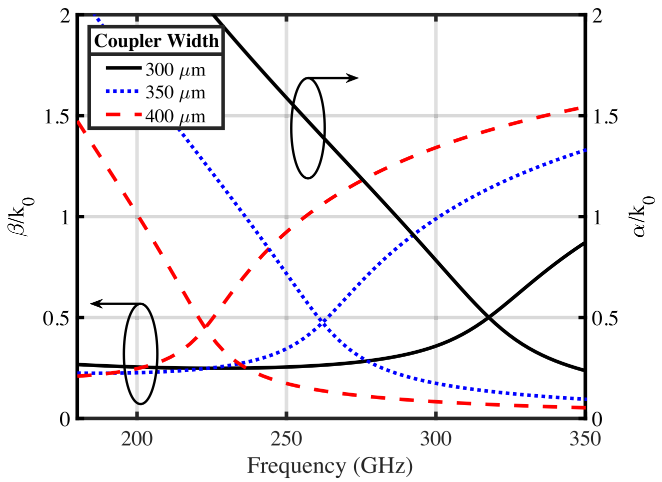

Fig. 6. Propagation constant of a uniform cross-sectional coupler for various coupler widths, $2d+a$, and gap width $a = 3.5$ μm from the analytical model.

dielectric, we assume k_x below the reference plane T and away from the slot is equal to k_y above T.

Considering the circuit model in Fig. 5(b), we can write the admittance looking down from the reference plane T as

$$Y_{\text{down}} = Y_{\text{TL}} + j(B_a + 2B_L) \tag{14}$$

and, similarly, the admittance looking up as

$$Y_{\text{up}} = \frac{1}{n_{\text{cs}}^2}(Y_c + jB_s). \tag{15}$$

In order for a transverse resonance to occur, we note that the phases of Y_{up} and Y_{down} at the resonance plane must cancel, from which we are able to solve for the transverse wavenumber in the horizontal portion of the coupler structure away from the slot

$$k_x = \sqrt{k_0^2\epsilon_r - k_z^2} \tag{16}$$

which in turn yields the longitudinal wavenumber, k_z, and subsequently, the propagation β and attenuation α constants.

C. Analytical Model: Numerical Investigation

In comparison to the case of an untapered structure, this tapered structure provides a progressively higher cutoff frequency as the wave travels longitudinally down the structure. In addition, the traveling wave also exhibits a commensurate increase in the rate of leakage α in the leaky regime. While an untapered structure will certainly leak energy into the covering semi-infinite dielectric, the length required to achieve high levels of coupling is much longer. In this way, the tapered structure is capable of forcing energy otherwise confined in a quasi-rectangular waveguide mode into a space leaky wave mode in a longitudinally shorter aperture while maintaining a large bandwidth.

Fig. 6 shows the dependence of the propagation constant β and attenuation constant α, as modeled in Section II-B, as a function of frequency for changing coupler widths. In this model, the dielectric into which the leaky wave is propagating is chosen to be compatible with the Rogers Corporation

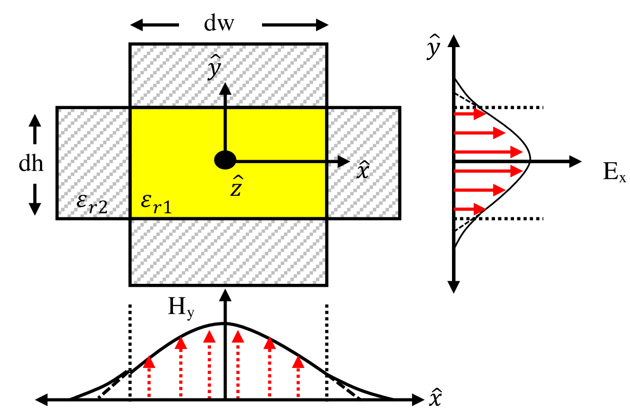

Fig. 7. Setup for Marcatili's rectangular dielectric guide approximation, and quasi-transverse E_{11}^x modes of a rectangular dielectric waveguide.

R3006 dielectric ($\epsilon_{r-\text{rad}} = 6.15$). From this plot, we can see that the analytical model predicts that, for a desired operating range of 220–320 GHz, the total guide width ranges from approximately 300–400 μm to provide leaky operation across the entire band, while maximizing leakage, α, for a given length. These values are utilized in a subsequent full-wave optimization as a starting point to co-optimize the dielectric waveguide cross section and the coupler geometry to minimize insertion loss and coupler return loss.

D. Dielectric Waveguide

Utilizing Marcatili's method [45] for rectangular waveguides, we consider a cross section of a homogenous dielectric material, size $dw \times dh$ μm^2 with dielectric constant ϵ_{r1} surrounded on each face, to ease analysis, by material, ϵ_{r2} (Fig. 7). This structure supports two quasi-transverse-electric modes, the E_{mn}^x and E_{mn}^y modes, in which the bulk of the field is polarized in either the $\hat{x}$ or $\hat{y}$ direction, respectively. The $\hat{x}$ polarized case, E_{11}^x is shown in Fig. 7. As in the case utilized in [15], we can set up the nonlinear relationships for the desired first order E_{11}^x mode, assuming the guide is surrounded by air ($\epsilon_{r2} = 1$) as

$$k_x dw = m\pi - 2\tan^{-1}\left(\frac{k_x}{\epsilon_{r1}\sqrt{k_0^2(\epsilon_{r1}-1) - k_x^2}}\right) \tag{17}$$

$$k_y dh = n\pi - 2\tan^{-1}\left(\frac{k_y}{\sqrt{k_0^2(\epsilon_{r1}-1) - k_y^2}}\right) \tag{18}$$

which can be solved for the transverse wavenumbers, k_x and k_y. From these, the dispersion relationship

$$k_z = \beta = \sqrt{\epsilon_{r1}k_0^2 - k_x^2 - k_y^2} \tag{19}$$

can be computed and used to determine the cutoff frequencies of a given mode. The cutoff frequencies of the first and second-order modes (E_{11}^x and E_{21}^x) are shown in Fig. 8(a) for a waveguide height, dh, of 250 μm thick bulk R3006 of different widths. In this case, an initial estimate of guide dimensions to preclude overmolding in the frequency band of choice can be

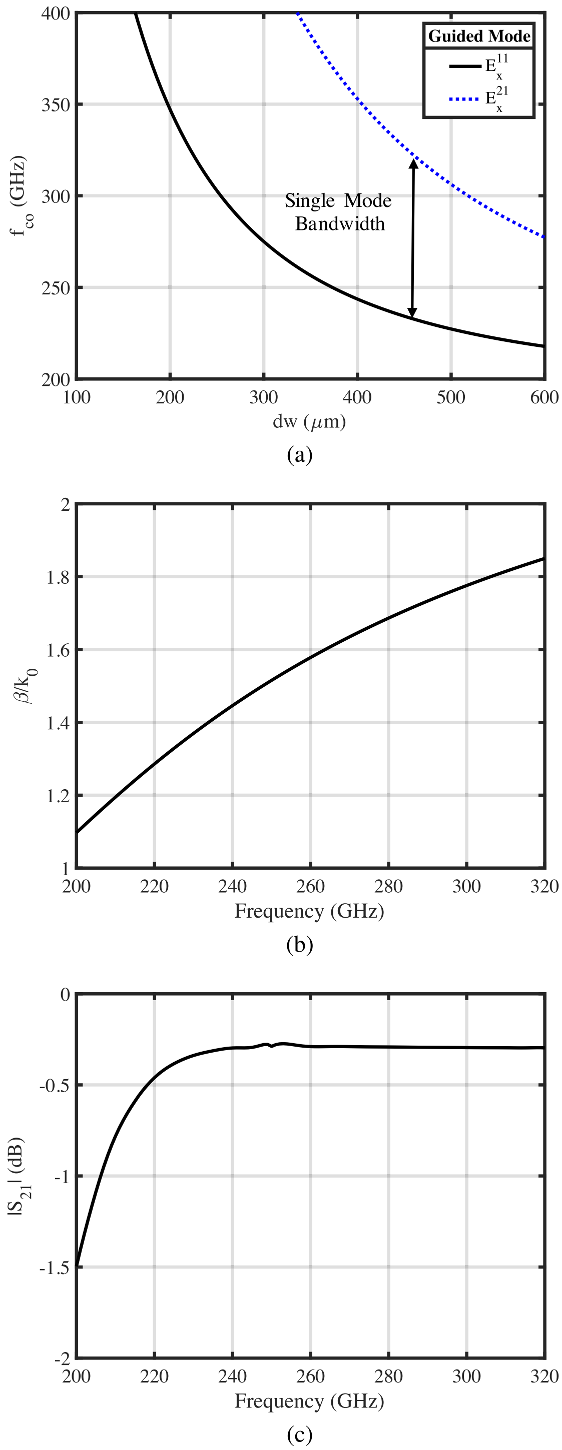

Fig. 8. (a) Predictions of the cutoff frequencies for the first and second order (E_{11}^x and E_{21}^x) modes of a $250 \times dw$ μm^2 R3006 dielectric waveguide guide from Marcatili's method, used as a starting point for full-wave optimization. (b) and (c) Full-wave data demonstrating operation above cutoff of the E_{11}^x mode in a 250×400 μm^2 cross-sectional R3006 waveguide of 500 mm in length.

made. This initial waveguide width, dw, of 500 μm was used in a full-wave simulation to co-optimize the coupler structure and the waveguide cross section. Following this optimization, a 400 μm waveguide width was chosen. As can be seen in Fig. 8(c) a 250×400 μm piece of the Rogers Corporation R3006 with a dielectric constant of 6.15 provides a more than

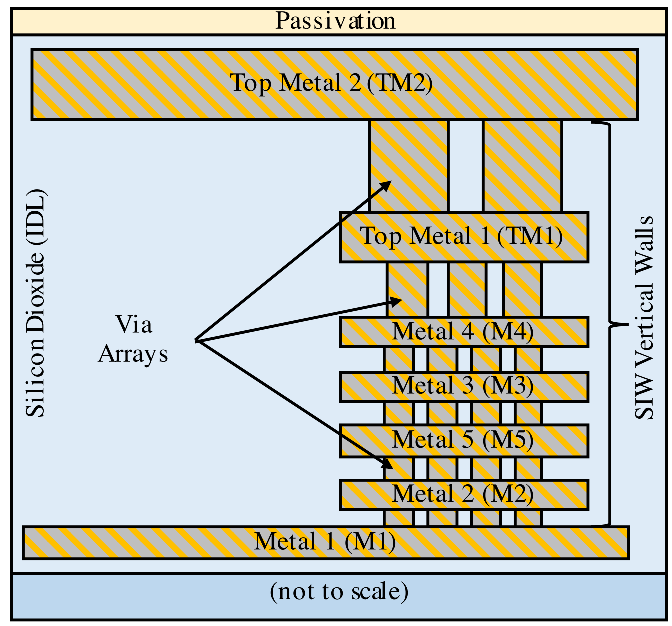

Fig. 9. Schematic of the IHP SG13G2 BEOL and substrate integrated waveguide structure (not to scale).

100 GHz of bandwidth from 220 GHz to beyond 320 GHz. It should be noted that Marcatili's approximation provides a reasonable starting point for full-wave electromagnetic simulation from which optimization is used to converge to a guide cross section that is mode-matched to the tapered coupler structure, maximizing power transfer.

E. On-Chip Tapered Coupler

Using the coupler dimensions derived numerically in Section II-C and the waveguide cross section in Section II-D as a starting point, the coupler and waveguide dimensions (L_{coupler}, a, and $a + 2d_w$ and $a + 2d_n$ at the coupler's wide and narrow widths, respectively) were designed in the IHP SG13G2 SiGe BiCMOS BEOL process and optimized with the aid of full-wave simulation tools. This process offers a 3 μm thick top metal with a distance of 9.83 μm between the top of the bottom metal and the bottom of the top metal. The coupler is composed of the bottom metal (Metal 1) and the top thick metal (Top Metal 2) as the horizontal conductors and the intermediate metal interconnects and arrays of vias to produce the vertical walls (Fig. 9).

A simplified model was implemented in HFSS, a commercial full-wave electromagnetic simulation package. The coupler geometry was excited by a 50 Ω source across the structure's slot at the wider end of the coupler (Fig. 2). Immediately on top of this coupler topology, a rectangular fiber with a thickness, dh, of 250 μm (to account for commercially available material thicknesses) rectangular cross-sectional fiber completely overlays the coupler slot and extends 500 μm beyond the narrow end of the structure. The second port of the model consists of a wave port at the end of this 500 μm protrusion. The coupler structure and waveguide dimensions

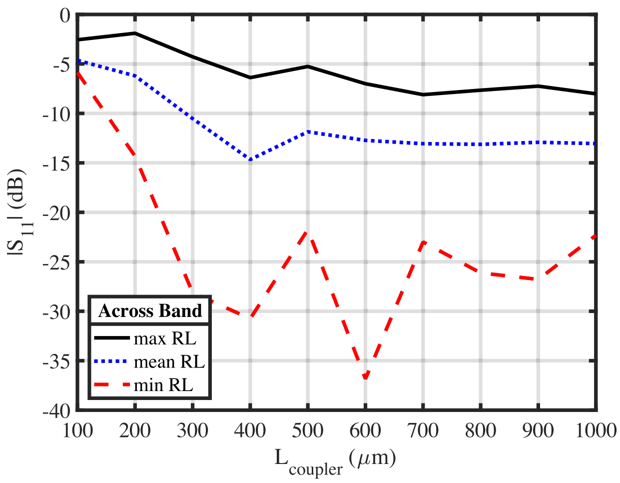

(a)

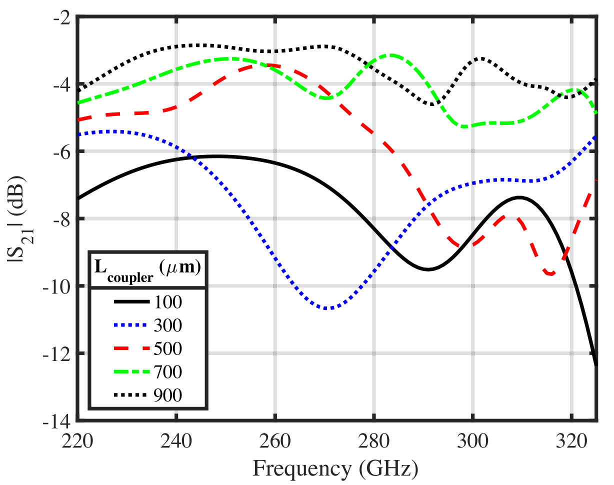

(b)

Fig. 10. Parametric full-wave analysis of the coupler structure radiating into a 250 × 400 μm^2 R3006 waveguide. (a) Magnitude of S_{11} (characteristic impedance 50 Ω). (b) Magnitude of S_{21} for various coupler lengths.

were optimized with $a \approx 3.5$ μm, $d_w \approx 180$ μm at the widest end of the structure, and $d_n \approx 100$ μm for the narrowest end of the structure to minimize the structure return and insertion loss across the desired 220–325 GHz operating band. From this point, full-wave simulations were executed to tune the coupler length, L_{Coupler}. The results of these simulations can be seen in Fig. 10. From these plots, one can readily see that the input match and insertion loss across the entire band improves with increasing coupler length. A coupler length, L_{coupler}, of 750 μm was chosen for fabrication to maintain an average insertion loss of approximately 4 dB with better than 8 dB of return loss across the band, while minimizing on-chip area.

III. Implementation

A. On-Die Structures

In order to facilitate on-wafer testing of the coupler, a mode converter (Fig. 11) was designed to provide a broadband conversion of an on-wafer 50 Ω microstrip mode to

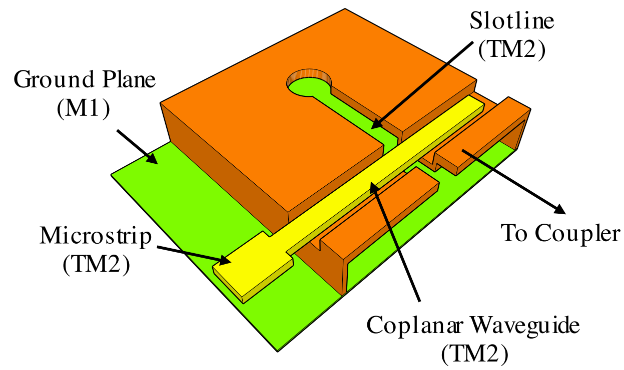

Fig. 11. Model of the mode-converter (not to scale). The vertical walls are modeled as solid and connected to the structure top metal (TM2). A continuous ground plane (M1) underneath the structure is shown. The feeding structure is illustrated as a microstrip connected to a coplanar waveguide (TM2).

a 50 Ω slot-line mode, driving the coupler structure (as shown schematically in Fig. 2). The microstrip feed line was implemented using the top and bottom metal layers, with a trace width of 17 μm. In addition, this mode-converter was used to compensate the slightly inductive input reactance of the coupler. By using Top Metal 1 (Fig. 9) under Top Metal 2 in the mode-converter feed structure, a capacitive waveguide E-plane iris is presented in parallel with the driving point of the coupler input [44], providing an improved input match. This section of the mode converter presents itself, essentially, as a grounded coplanar waveguide (GCPW) or half of a rectangular coaxial transmission line with a trace width of 4 μm, and a gap width of 20 μm. The distance between the bottom of the signal trace and the GCPW effective ground is 3 μm. The mode converter is approximately a quarter-wave in length at the center of the operating band, comprised of a 170 μm long 3.5 μm wide slot and a 20 μm diameter circular choke for broadband response. This mode converter is designed with the same cross section (width, height, gap width, etc.) as the coupler structure, enabling direct connection to the coupler structure. With the integration of on-chip electronics, this mode-converter may not be necessary, further decreasing the end-to-end insertion loss and reducing the overall coupler size.

On-die calibration standards were designed and implemented, enabling multiline transmission, reflection, and line (mTRL) calibration [46]. Microstrip lines of lengths commensurate with those driving the coupler and mode-converter structures were available on die to aid in de-embedding the microstrip loss. Lastly, a back-to-back mode-converter was implemented on die to enable de-embedding the response associated with the mode-conversion and subsequent additional dielectric and ohmic losses. A microphotograph of the taped-out chip is presented in Fig. 12. The entire chip is 2.0 × 2.0 mm^2 and requires no postprocessing or special handling.

B. Test Coupon and Dielectric Waveguide

A test coupon/holder was designed (Fig. 13) to provide a rigid substrate, maintaining relative position between two

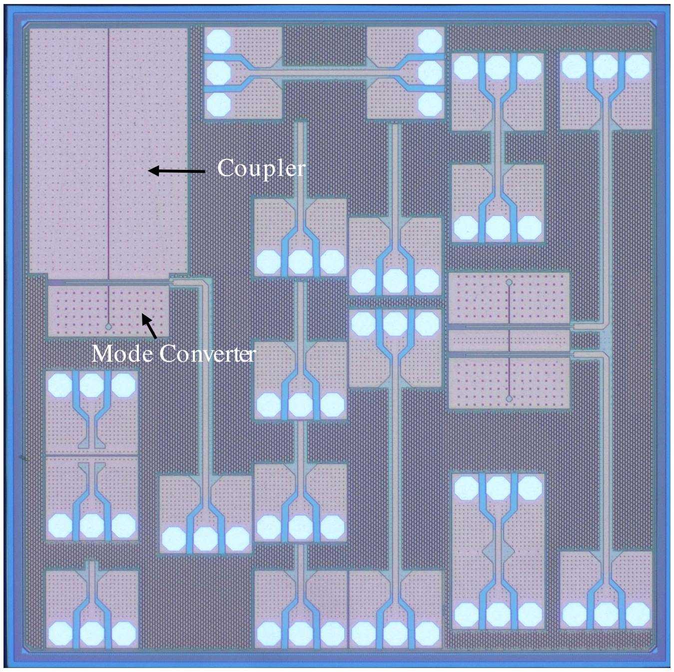

Fig. 12. Die photograph of the chip, including calibration standards, de-embedding structures, and the coupler.

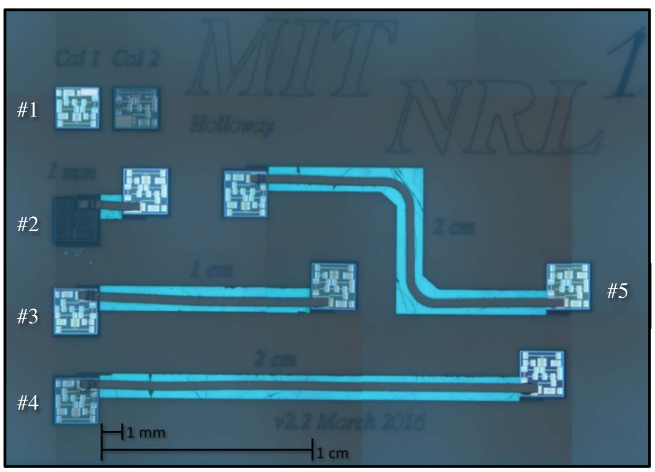

Fig. 13. Photograph of a fully populated test coupon (the light blue areas are from back-side illumination on the micrograph station).

dies under test. This substrate provided a stable platform onto which dies were bonded, and subsequently, the dielectric waveguides bonded to these dies. In order to minimize evanescent mode coupling into areas surrounding the dielectric waveguide a low dielectric constant Rogers TMM3 ceramic composite material ($\epsilon_r \approx 3.27$) was selected for the substrate. The material was laser ablated for individual die position, depressed 300 μm from the material surface. Areas underneath the desired dielectric waveguide routing were removed to reduce the waveguide's evanescent field interaction with the substrate. The final test coupon consists of three straight waveguide sections of different lengths and one section that has two 90° bends with a radius of 1.2 mm. Table I enumerates the waveguide lengths corresponding to those positions in Fig. 13.

TABLE I
TEST COUPON POSITIONS AND WAVEGUIDE LENGTHS

Position in Fig. 13	Chip-to-Chip Distance	Notes
1	N/A	Calibration Positions
2	0.1 cm	Straight Waveguide
3	1.0 cm	Straight Waveguide
4	2.0 cm	Straight Waveguide
5	2.0 cm	2 x 90° Bends, 1.2 mm Rad. of Curve

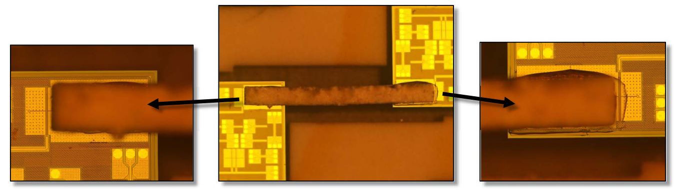

Fig. 14. Bonding of the dielectric waveguide to coupler apertures.

Rogers R3006 was chosen for the dielectric waveguide interconnect for its specified dielectric constant, machinability, low loss, and wide availability. These waveguides were made from bulk 250 μm thick unclad R3006 that are laser cut to a width, dw, of 400 ± 10 μm. A number of straight and curved waveguide pieces were cut to align with the individual die and coupler positions after bonding to the test coupon/substrate described in the next section.

After the individual dies were placed, aligned, and bonded to the substrate material, the dielectric waveguides were then individually bonded on top of the chips' passivation layers (Fig. 14) with EPOTEK 713 epoxy. Following the preparation of the test coupon substrate, die bonding, and waveguide bonding, the vertical relief of the bonds was investigated using a microscope profilometer. We were able to measure the distance between the top of the individual die passivation layer and the bottom of the dielectric waveguide (denoted as ΔH_{gap}) at each position. At positions #2, #3, and #5, we found that the bond was flush with the top of the passivation layer ($\Delta H_{\text{gap}} \approx 0$ μm), whereas the bonds for the 2 cm straight waveguide, position #4, had an average separation of approximately 17.5 μm above the two chip interfaces. Our inability to remove the epoxy and waveguide from these positions without damage and our limited number of dies precluded rebonding these positions. As such, a full-wave characterization of the effects of this separation was carried out over the frequency range 220–320 GHz. The results of this simulation (Fig. 15) show that approximately 2.5 dB increased loss, averaged across the band, is expected in the measurement of position #4.

IV. MEASUREMENT

A. *Setup*

Calibrations and measurements of these coupons were taken using a SUSS microprobe station with micropositioners, an Agilent N5426 PNA-X network analyzer, a set of OML WR-3.4 220–325 GHz VNA extenders, and two Cascade Infinity ground-signal-ground probes (Fig. 16). A second set

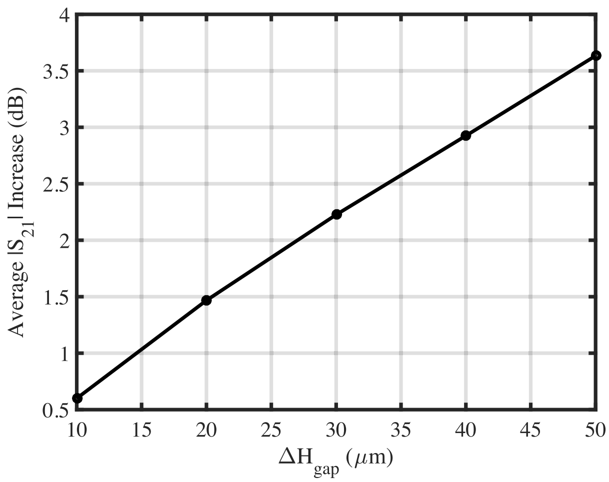

Fig. 15. Full-wave simulation results of the increase in insertion loss, averaged over the frequency band, of a single coupler-waveguide transition as a function of ΔH_{gap}.

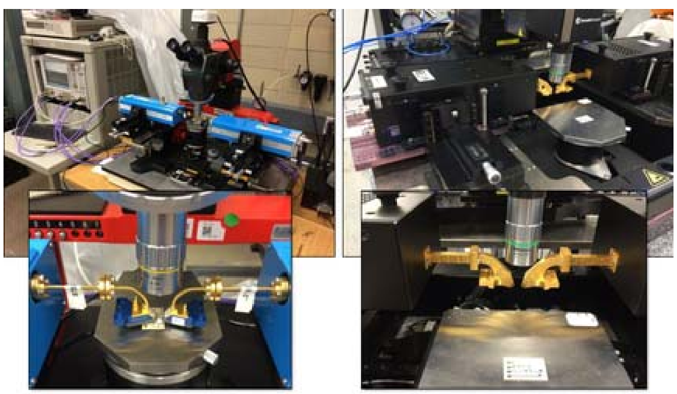

Fig. 16. Measurement setup utilizing OML frequency extenders with Cascade Infinity probes (left), and VDI extenders with DMPI T-Wave probes (right).

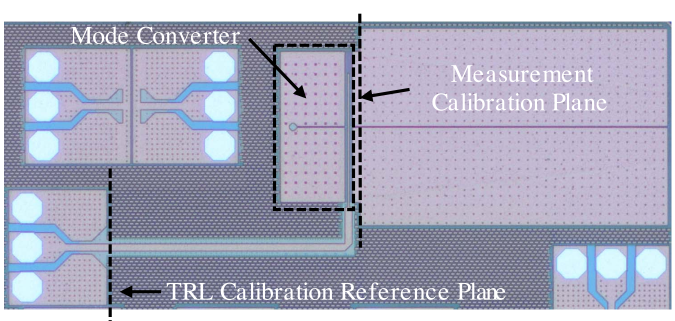

Fig. 17. Calibration reference plane following mTRL calibration.

of measurements was taken to verify these measurements with Virginia Diodes, Inc. frequency extenders and Dominion Microprobe's T-Wave probes.

B. De-Embedding

A multiline thru-reflect-line (mTRL) calibration [46], using on-chip calibration standards, was used to establish the calibration plane at the beginning of the microstrip transmission line

TABLE II

SUMMARY OF MEASURED AND SIMULATED COUPLER RESPONSES FROM 220 TO 270 GHz

Average Coupler-Waveguide-Coupler Loss		
Guide Length	Measured	Simulated
0.1 cm	6.2 dB	7.7 dB
1.0 cm	10.2 dB	7.4 dB
straight 2.0 cm	12.2 dB	11.4 dB
bent 2.0 cm	10.7 dB	7.5 dB

TABLE III

COMPARISON OF THE PRESENTED WORK WITH PUBLISHED mmWAVE/SUB-mmWAVE RADIO OVER FIBER COUPLERS

Ref.	This Work	[3]	[13]	[16]	[15]
Center Freqs.	275 GHz	195 GHz	77 GHz 75 GHz	60 GHz	57 GHz 80 GHZ
BW	50 GHz	8 GHz	35 GHz	6 GHz	6 GHz
Ins. Loss	4.8 dB	5.8 dB	5 dB	6 dB	7 dB (est)
Guide Cross Section	400 μm 250 μm	500 μm 300 μm	850 μm 850 μm	1.6 mm Radius	1.1 mm 8 mm
Notes	1	2	3	2	3

1 On-chip coupler with a planar chip-waveguide interface
2 On-chip coupler with the waveguide attached to the chip at a 90° angle
3 Off-chip coupler with a planar chip-waveguide interface

shown in Fig. 17. Good calibrations were repeatably obtained from 220 to 270 GHz. Above 270 GHz, an unanticipated resonance appeared, which is due to unpredicted coupling with the BEOL dummy metal fill around the pads and transmission lines added by the fab to adhere to minimum metal density rules. Postcalibration measurements of microstrip transmission lines and mode-converter de-embedding structures were taken to enable de-embedding of the coupler structure and waveguide response.

C. Results

Utilizing the microstrip and mode-converter de-embedding structure responses, the back-to-back coupler-to-waveguide response was de-embedded from measurement. The resultant de-embedded data are presented in Fig. 18. The presented data are calibrated to the reference plane between the mode converter and the coupler structure (Fig. 17). The phase in Fig. 18(c) is not the absolute phase shift of each coupler-waveguide-coupler transmission, but rather is reduced by a multiple of 360° so that the phase at 220 GHz lies within 0°–360°, as directly provided by the VNA in the measurement.

Compared to the 2.0 cm waveguide with bends, the 2.0 cm straight waveguide has an additional measured average insertion loss of 2.5 dB, partly due to the 17.5 μm ΔH_{gap}. The simulated loss increase corresponding to ΔH_{gap} is shown in Fig. 15. The significantly reduced insertion loss and increased phase delay of the 0.1 cm waveguide compared to the longer waveguides indicated that this length is short enough to support energy coupling into not only a traveling wave mode in the dielectric guide, but a radiative mode coupled into the opposite side of the link.

The close and linear relationship between the phase responses, normalized to the waveguide lengths, indicates

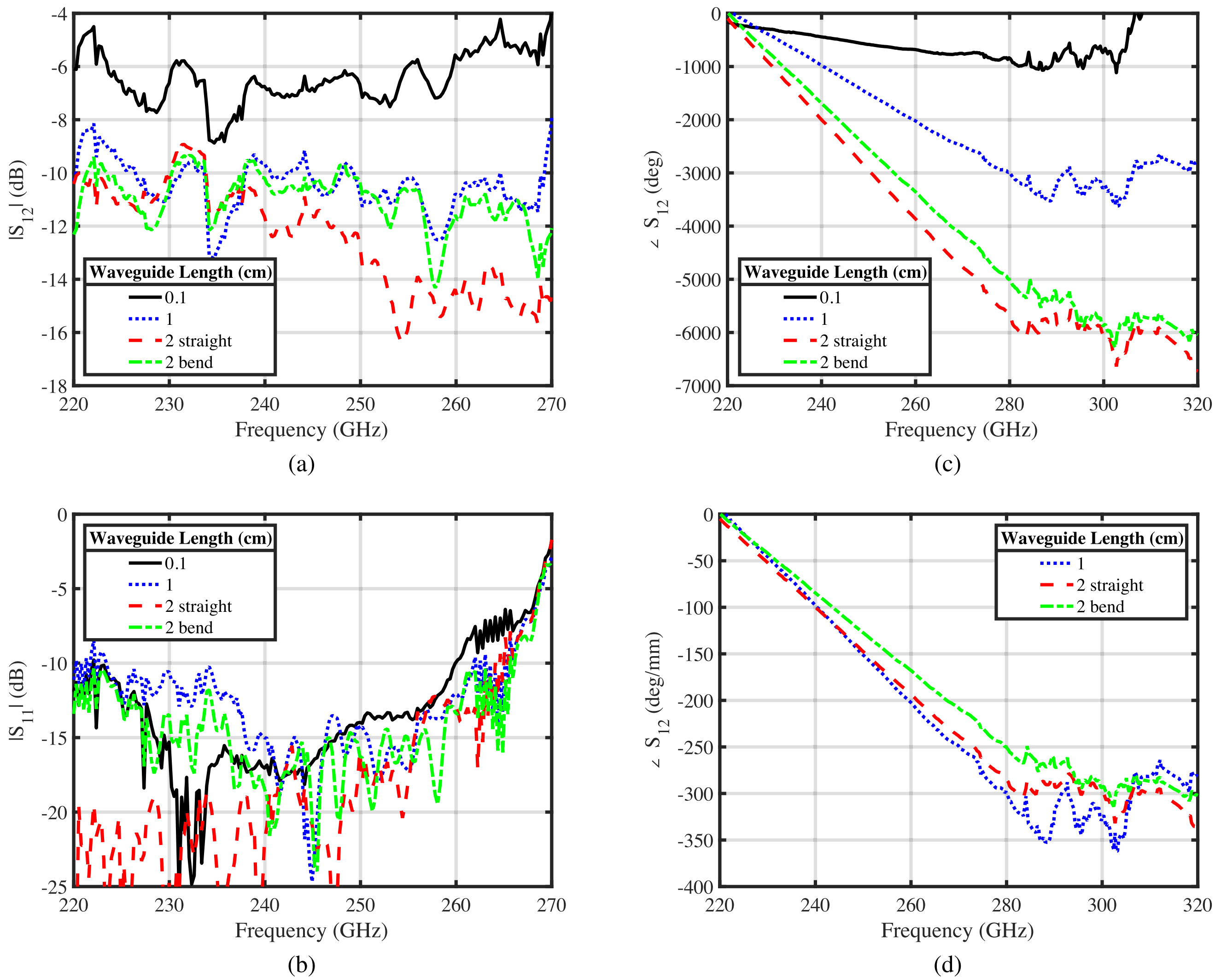

Fig. 18. Measured coupler-waveguide-coupler response (a) and (b) S-parameter magnitude response, (c) phase response, and (d) length-normalized phase response for measured waveguide lengths.

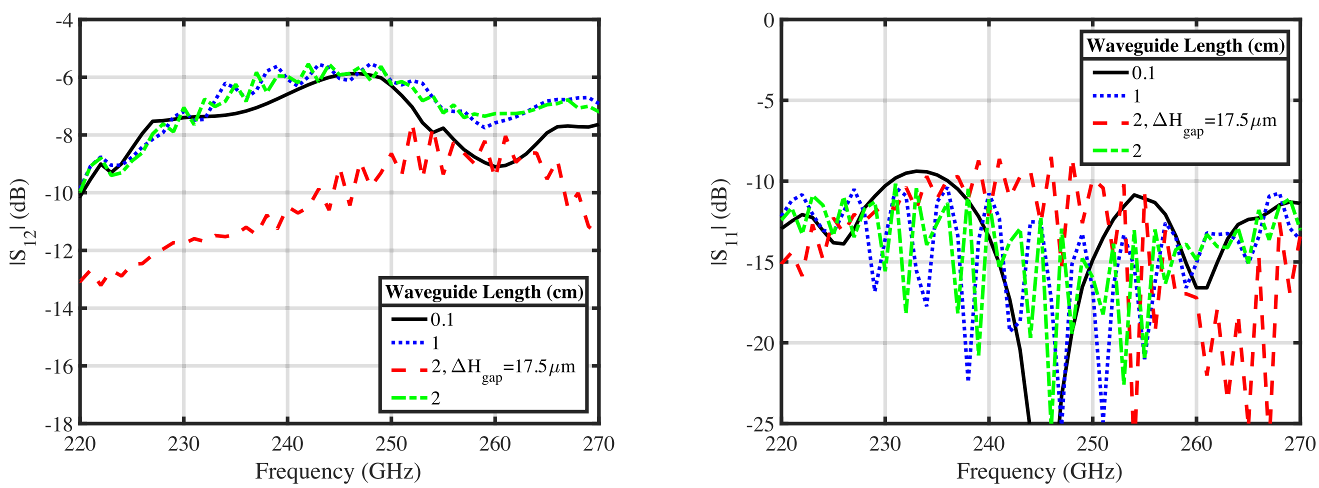

Fig. 19. Full-wave simulated coupler-fiber-coupler response with straight 0.1, 1.0, and 2.0 cm waveguide lengths. The 2.0 cm guide is also simulated with gap between the waveguide and coupler surface, ΔH_{gap}, of 17.5 μm to compare with measured data. The simulated coupler and waveguide dimensions are identical to those used in the measurements.

that the guided waves do not encounter significant dispersion along the waveguide. A flat group delay of approximately 14 ps/mm was measured. For comparison, full-wave coupler-waveguide-coupler simulation results are provided in Fig. 19. The average measured and simulated coupler-waveguide loss is presented in Table II. The discrepancy between simulated and measured data is attributed to additional waveguide dielectric loss at sub-mmWave frequencies, measurement inaccuracies, and imperfect waveguide-chip bonding. Lastly, it should be noted that, after accounting for the excess coupling loss present in the 2.0 cm straight guide sample bonds, the 1.0 and 2.0 cm average losses over the band are currently estimated at only 0.5 dB/cm. Given this waveguide loss, we estimate the insertion loss of a single coupler is approximately 4.8 dB which agrees well with the simulated data of approximately 3.8 dB per transition. The performance of this interchip link system exceeds that of the previous state-of-the-art results. A comparison of available "radio of fiber" coupler performance is provided in Table III.

V. Conclusion

In this paper, a fully integrated on-chip traveling wave power coupler, based on a differentially driven HM-SIW structure, codesigned with a low-cost planar rectangular dielectric waveguide is presented, analyzed, and measured. This structure achieves an insertion loss of 4.8 dB, which is the lowest among all published works in the millimeter-wave frequency band. The increased operating frequency provides the smallest waveguide cross section and the potential for a lower guide-to-guide pitch. A usable bandwidth of 50 GHz was measured, providing an opportunity for very high data rate transmission. This structure provides the most straightforward path for on-chip integration. The proposed coupler structure also enables the simplest implementation of a planar interface between the chip and dielectric waveguide. This simple system-level planar integration makes use of low-cost commercially available materials already in widespread use in the PCB industry.

To the best of the authors' knowledge, this structure is demonstrated for the first time at these frequencies, providing smaller guide size, lower pitch, and more available bandwidth than demonstrated in previously published works. Lastly, the small differences in losses between the 1.0 and 2.0 cm samples indicates low loss in this guide material at these frequencies, approximately 0.5 dB/cm. This in-guide loss makes this design viable for link lengths up to approximately one meter.

Appendix
Theoretical Link Efficiency

Assuming BPSK modulation and an AWGN channel, we define the bit error rate (BER) as the probability

$$Q(A) = \frac{1}{\sqrt{2\pi}} \int_A^\infty e^{-\frac{x^2}{2}} dx \tag{20}$$

where the substitution

$$A = \sqrt{2\gamma_b} \tag{21}$$

corresponds to a signal-to-noise ratio (SNR) per bit of

$$\gamma_b = \frac{E_b}{N_0}. \tag{22}$$

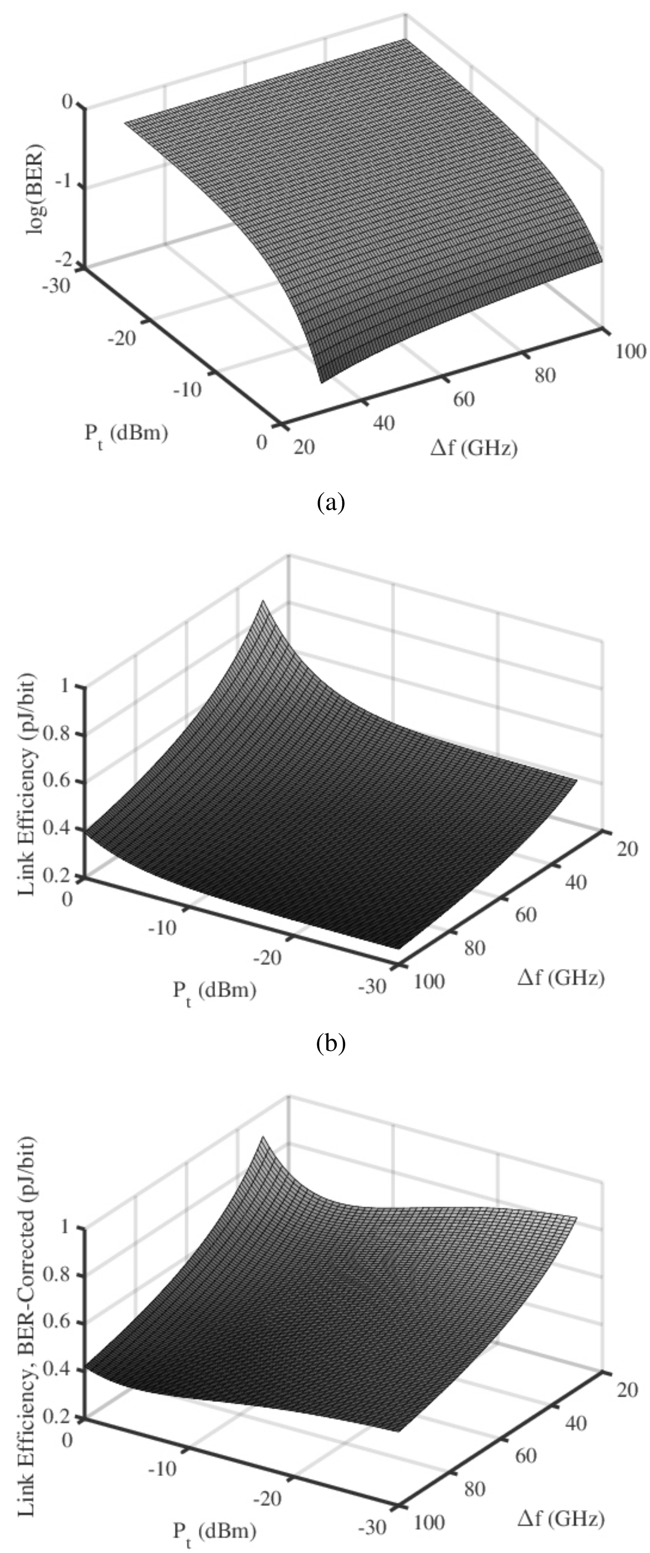

(a)

(b)

(c)

Fig. 20. Theoretical BPSK sub-mmWave link as a function of available bandwidth Δf and transmitted power P_t (a) BER, (b) link efficiency, and (c) link efficiency accounting for overhead associated with BER.

Given a detector NEP, we can write the required receive power P_r for a given SNR and bandwidth Δf as

$$P_r = \text{SNR} \cdot \text{NEP} \cdot \sqrt{\Delta f}. \tag{23}$$

In addition, we know that the theoretical Shannon capacity C for this channel model can be written as

$$C = \Delta f \cdot \log_2(1 + \mathrm{SNR}). \tag{24}$$

Assuming a coupling loss L_c and a loss associated with some length of waveguide L_d, we know that the received power is related to the transmit power

$$P_r = P_t - L_d - 2L_c \text{ (dBm)} \tag{25}$$

and lastly, given a dc-to-RF conversion efficiency η, if we assume that the power generation efficiency dominates the total transmit-receive chain, we can characterize the theoretical capacity, BER, and the link efficiency. In addition, we characterize an effective capacity, in which the effects of BER are accounted for as

$$C_e = C \cdot (1 - \mathrm{BER}). \tag{26}$$

The results are plotted in Fig. 20 for a range of transmit powers and available bandwidths, assuming a 2.4% dc-to-RF conversion efficiency, a 29 pW/$\sqrt{\mathrm{Hz}}$ detector NEP, and a total loss, $L_d + 2L_c$, of 20 dB.

From this figure, we can see that, for a 50 GHz bandwidth, as demonstrated in this paper, with a 0 dBm transmit power and a 20 cm link, theoretical link efficiency is as high as 67.3 or 63.1 Gb/s when accounting for a BER of $61.5 \cdot 10^{-3}$. These figures correspond to a -20 dBm received power and a transmitter dc power of 416.7 mW.

Acknowledgment

The authors would like to thank Dominion Microprobes Inc., Virginia Diodes Inc., and the Rogers Corporation for testing and material support. The authors would also like to thank Dr. H. Newman, Dr. S. Shin, J. Rousseau, and Dr. E. Naglich of the Naval Research Laboratory, Code 6850, and Dr. C. Galbraith at MIT Lincoln Laboratory for equipment support and a number of discussions.

The views, opinions, and/or findings contained in this paper are those of the authors and should not be interpreted as representing the official views or policies, either expressed or implied, of the Office of Naval Research or the Department of Defense.

References

[1] W. Liu *et al.*, "Exploration of electrical and novel optical chip-to-chip interconnects," *IEEE Des. Test.*, vol. 31, no. 5, pp. 28–35, Oct. 2014.

[2] V. Kumar, R. Bashirullah, and A. Naeemi, "Modeling, optimization and benchmarking of chip-to-chip electrical interconnects with low loss air-clad dielectrics," in *Proc. IEEE 61st Electron. Compon. Technol. Conf. (ECTC)*, May 2011, pp. 2084–2090.

[3] Q. J. Gu, "THz interconnect: The last centimeter communication," *IEEE Commun. Mag.*, vol. 53, no. 4, pp. 206–215, Apr. 2015.

[4] A. E.-J. Lim *et al.*, "Review of silicon photonics foundry efforts," *IEEE J. Sel. Topics Quantum Electron.*, vol. 20, no. 4, Jul./Aug. 2014, Art. no. 8300112.

[5] J. S. Orcutt and R. J. Ram, "Photonic device layout within the foundry CMOS design environment," *IEEE Photon. Technol. Lett.*, vol. 22, no. 8, pp. 544–546, Apr. 15, 2010.

[6] J. Michel and L. C. Kimerling, "Electronics and photonics: Convergence on a silicon platform," in *Proc. 33rd Eur. Conf. Ehxibit. Opt. Commun. (ECOC)*, Sep. 2007, pp. 1–2.

[7] D. J. Shin *et al.*, "Integration of silicon photonics into DRAM process," in *Proc. Opt. Fiber Commun. Conf. Expo. Nat. Fiber Opt. Eng. Conf. (OFC/NFOEC)*, Mar. 2013, pp. 1–3.

[8] C. Sun *et al.*, "A monolithically-integrated chip-to-chip optical link in bulk CMOS," *IEEE J. Solid-State Circuits*, vol. 50, no. 4, pp. 828–844, Apr. 2015.

[9] P. Markov, J. G. Valentine, and S. M. Weiss, "Fiber-to-chip coupler designed using an optical transformation," *Opt. Exp.*, vol. 20, no. 13, pp. 14705–14713, Jun. 2012.

[10] A. Mekis *et al.*, "A grating-coupler-enabled CMOS photonics platform," *IEEE J. Sel. Topics Quantum Electron.*, vol. 17, no. 3, pp. 597–608, May/Jun. 2011.

[11] G. Roelkens, P. Dumon, W. Bogaerts, D. Van Thourhout, and R. Baets, "Efficient fiber to SOI photonic wire coupler fabricated using standard CMOS technology," in *Proc. 18th Annu. Meeting IEEE Lasers Elect.-Opt. Soc. (LEOS)*, Oct. 2005, pp. 197–198.

[12] A. Khilo, M. A. Popović, M. Araghchini, and F. X. Kartner, "Efficient planar fiber-to-chip coupler based on two-stage adiabatic evolution," *Opt. Exp.*, vol. 18, no. 15, pp. 15790–15806, 2010.

[13] A. Arbabian, N. Dolatsha, and N. Saiz, "Fully packaged millimetre-wave dielectric waveguide with multimodal excitation," *IEEE Electron. Lett.*, vol. 51, no. 17, pp. 1339–1341, Aug. 2015.

[14] N. Dolatsha and A. Arbabian, "Analysis and design of multi-mode dielectric waveguide interconnect with planar excitation," in *Proc. PIERS*, Aug. 2013, pp. 234–239.

[15] S. Fukuda *et al.*, "A 12.5+12.5 Gb/s full-duplex plastic waveguide interconnect," *IEEE Int. Solid-State Circuits*, vol. 46, no. 12, pp. 3113–3125, Dec. 2011.

[16] Y. Kim, L. Nan, J. Cong, and M.-C. F. Chang, "High-speed mm-wave data-link based on hollow plastic cable and CMOS transceiver," *IEEE Microw. Wireless Compon. Lett.*, vol. 23, no. 12, pp. 674–676, Dec. 2013.

[17] W. Volkaerts, N. Van Thienen, and P. Reynaert, "An FSK plastic waveguide communication link in 40 nm CMOS," in *IEEE Int. Solid-State Circuits Conf. (ISSCC) Dig. Tech. Papers*, Feb. 2015, pp. 1–3.

[18] B. Yu, Y. Liu, Y. Ye, J. Ren, X. Liu, and Q. J. Gu, "High-efficiency micromachined sub-THz channels for low-cost interconnect for planar integrated circuits," *IEEE Trans. Microw. Theory Techn.*, vol. 64, no. 1, pp. 96–105, Jan. 2016.

[19] N. Dolatsha and A. Arbabian, "Dielectric waveguide with planar multimode excitation for high data-rate chip-to-chip interconnects," in *Proc. IEEE Int. Conf. Ultra-Wideband (ICUWB)*, Sep. 2013, pp. 184–188.

[20] D. P. Kopp, M. A. A. Khan, G. H. Bernstein, and P. Fay, "Ultra-broadband chip-to-chip interconnects to 220 GHz for Si-based millimeter-wave systems," in *Proc. IEEE Int. Interconnect Technol. Conf./Adv. Metallization Conf. (IITC/AMC)*, May 2014, pp. 293–296.

[21] A. Malekabadi, S. A. Charlebois, D. Deslandes, and F. Boone, "High-resistivity silicon dielectric ribbon waveguide for single-mode low-loss propagation at F/G-bands," *IEEE Trans. THz Sci. Technol.*, vol. 4, no. 4, pp. 447–453, Jul. 2014.

[22] M. Tytgat and P. Reynaert, "A plastic waveguide receiver in 40nm CMOS with on-chip bondwire antenna," in *Proc. ESSCIRC (ESSCIRC)*, Sep. 2013, pp. 335–338.

[23] A. Hajimiri, "mm-Wave silicon ICs: Challenges and opportunities," in *Proc. IEEE Custom Integr. Circuits Conf. (CICC)*, Sep. 2007, pp. 741–747.

[24] G. M. Rebeiz, "Millimeter-wave and terahertz integrated circuit antennas," *Proc. IEEE*, vol. 80, no. 11, pp. 1748–1770, Nov. 1992.

[25] E. Afshari and R. Han, "Progress towards mW-power generation in CMOS THz signal sources," in *Proc. Eur. Microw. Integr. Circuits Conf. (EuMIC)*, Oct. 2013, pp. 117–120.

[26] C. Jiang, A. Cathelin, and E. Afshari, "An efficient 210 GHz compact harmonic oscillator with 1.4 dBm peak output power and 10.6% tuning range in 130 nm BiCMOS," in *Proc. IEEE Radio Freq. Integr. Circuits Symp. (RFIC)*, May 2016, pp. 194–197.

[27] R. Han *et al.*, "A 280-GHz Schottky diode detector in 130-nm digital CMOS," *IEEE J. Solid-State Circuits*, vol. 46, no. 11, pp. 2602–2612, Nov. 2011.

[28] P. Kumar, "Comparative analysis of BER performance for direct detection and coherent detection FSO communication systems," in *Proc. 5th Int. Conf. Commun. Syst. Netw. Technol. (CSNT)*, Apr. 2015, pp. 369–374.

[29] R. Han *et al.*, "A SiGe terahertz heterodyne imaging transmitter with 3.3 mW radiated power and fully-integrated phase-locked loop," *IEEE J. Solid-State Circuits*, vol. 50, no. 12, pp. 2935–2947, Dec. 2015.

[30] J.-D. Park and A. M. Niknejad, "Y-band on-chip dual half-width leaky-wave antenna in a nanoscale CMOS process," *IEEE Antennas Wireless Propag. Lett.*, vol. 12, pp. 1476–1479, 2013.
[31] F. Gutierrez, S. Agarwal, K. Parrish, and T. S. Rappaport, "On-chip integrated antenna structures in CMOS for 60 GHz WPAN systems," *IEEE J. Solid-State Circuits*, vol. 27, no. 8, pp. 1367–1378, Oct. 2009.
[32] G. Q. Luo, "Low profile cavity backed antennas based on substrate integrated waveguide technology," in *Proc. IEEE Asia–Pacific Conf. Antennas Propag. (APCAP)*, Aug. 2012, pp. 275–276.
[33] T. Y. Yang, W. Hong, and Y. Zhang, "Wideband millimeter-wave substrate integrated waveguide cavity-backed rectangular patch antenna," *IEEE Antennas Wireless Propag. Lett.*, vol. 13, pp. 205–208, 2014.
[34] N. J. Karl, R. W. Mckinney, Y. Monnai, R. Mendis, and D. M. Mittleman, "Frequency-division multiplexing in the terahertz range using a leaky-wave antenna," *Nature Photon.*, vol. 9, pp. 717–720, Sep. 2015.
[35] L. O. Goldstone and A. A. Oliner, "Leaky-wave antennas I: Rectangular waveguides," *IRE Trans. Antennas Propag.*, vol. 7, no. 4, pp. 307–319, Oct. 1959.
[36] A. A. Oliner and P. Lampariello, "The dominant mode properties of open groove guide: An improved solution," *IEEE Trans. Microw. Theory Techn.*, vol. 33, no. 9, pp. 755–764, Sep. 1985.
[37] A. A. Oliner, "Scannable millimeter wave arrays," DTIC/USAF Rome Air Development Center, Tech. Rep., 1989. [Online]. Available: http://dtic.mil/dtic/
[38] G.-F. Cheng and C.-K. C. Tzuang, "A differentially excited coupled half-width microstrip leaky EH_1 mode antenna," *IEEE Trans. Antennas Propag.*, vol. 61, no. 12, pp. 5885–5892, Dec. 2013.
[39] I. V. Lindell, A. H. Sihvola, and I. Hänninen, "Realization of perfectly anisotropic impedance boundary," in *Proc. 1st Eur. Conf. Antennas Propag. (EuCAP)*, Nov. 2006, pp. 1–4.
[40] J. Zehentner, J. Machác, and P. Zabloudil, "Low profile slotted flat waveguide leaky wave antenna," in *IEEE MTT-S Int. Microw. Symp. Dig.*, Jun. 2006, pp. 1303–1306.
[41] J. Zehentner, J. Machac, and J. Mrkvica, "Planar transmission lines in MW and MMW circuits," in *Proc. 7th Int. Conf. Telecommun. Modern Satellite, Cable Broadcast. Services*, Sep. 2005, pp. P-III–PP-XI.
[42] C. M. Krowne, "Approximations to hybrid mode slot line behaviour," *Electron. Lett.*, vol. 14, no. 8, pp. 258–259, Apr. 1978.
[43] P. Lampariello and A. A. Oliner, "New equivalent networks with simple closed-form expressions for open and slit-coupled E-plane tee junctions," *IEEE Trans. Microw. Theory Techn.*, vol. 41, no. 5, pp. 839–847, May 1993.
[44] N. Marcuvitz, *Waveguide Handbook*. New York, NY, USA: Dover, 1965.
[45] E. A. J. Marcatili, "Dielectric rectangular waveguide and directional coupler for integrated optics," *Bell Syst. Tech. J.*, vol. 48, no. 7, pp. 2071–2102, Sep. 1969.
[46] D. F. Williams, A. C. Young, and M. Urteaga, "A prescription for sub-millimeter-wave transistor characterization," *IEEE Trans. THz Sci. Technol.*, vol. 3, no. 4, pp. 433–439, Jul. 2013.

Jack W. Holloway (S'03) was born in Colby, Thomas County, KS, USA, in 1980. He received the S.B. degrees in applied mathematics and electrical engineering and M.Eng. degree in electrical engineering and computer science from the Massachusetts Institute of Technology (MIT), Cambridge, MA, USA, in 2003 and 2004, respectively, where he is currently pursuing the Ph.D. degree in integrated terahertz circuit design with the MIT Microsystems Technology Laboratory.

Since 2006 he has been an Officer with the United States Marine Corps, where he has been an F/A-18 Pilot since 2010. Currently, he is with the Office of Naval Research, Arlington, VA, USA, as a Science and Technology Program Officer at the Expeditionary Maneuver Warfare and Combating Terrorism Department (Code 30).

Mr. Holloway is an MIT Lincoln Laboratory Military Fellow.

Luciano Boglione (M'98–SM'07) received the Ph.D. degree (with a focus on low-noise amplifier design under the supervision of the late Prof. R. Pollard) from The University of Leeds, Leeds, U.K., in 1998.

He possesses 20 years of experience in the design and characterization of monolithic microwave and radio frequency integrated circuits (IC) fabricated in Silicon and compound semiconductor technologies. His professional experience embraces industry, academia, and government institutions. In 2011, he joined the Naval Research Laboratory, Washington, DC, USA, where he has been involved in noise theory and characterization of linear devices and IC designs in advanced technologies for broadband, high-frequency applications. He has authored more than 20 papers in peer-reviewed publications.

Dr. Boglione was the General Chair of the 2007 IEEE RFIC Symposium and is an active IEEE MTT-S volunteer.

Timothy M. Hancock (S'96–M'05–SM'11) received the B.S. degree in electrical engineering from the Rose-Hulman Institute of Technology, Terre Haute, IN, USA, and the M.S. and Ph.D. degrees in electrical engineering from the University of Michigan, Ann Arbor, MI, USA, where he was involved in the development of SiGe integrated microwave circuits from 6 to 77 GHz.

He was with Conexant Systems, with a focus on a single-chip GPS receiver and at M/A-COM on a silicon germanium 24 GHz automotive radar solution. From 2005 to 2011, he was a Staff Member with the Analog Device Technology Group, MIT Lincoln Laboratory, Massachusetts Institute of Technology (MIT), Cambridge, MA, USA, where he was involved in the development of low-power, small form-factor wireless devices, and reconfigurable and multiple-input-multiple-output (MIMO) communication systems, and focused on integrated circuit design and wireless system design. From 2011 to 2016, he was an Assistant Leader with the RF Technology Group, where he developed and managed programs on wide range of topics including MIMO communications, wideband receiver technology for RADAR and ELINT systems, millimeter wave hyperspectral cubesat-based radiometers, compound semiconductor material growth, and device process development. Currently he is on a leave of absence from the MIT Lincoln Laboratory to serve as a Program Manager with the Defense Advanced Research Projects Agency in the Microsystems Technology Office. He has authored more than 20 papers.

Dr. Hancock served for ten years on the Technical Program Committee of the Radio Frequency Integrated Circuits Symposium before retiring from this role and has been an active member of the Boston International Microwave Symposium Steering Committees. He was the 2010 inaugural recipient of the MIT Lincoln Laboratory Early Career Technical Achievement Award.

Ruonan Han (S'10–M'14) received the B.Sc. degree in microelectronics from Fudan University, Shanghai, China, in 2007, the M.Sc. degree in electrical engineering from the University of Florida, Gainesville, FL, USA, in 2009, and the Ph.D. degree in electrical and computer engineering from Cornell University, Ithaca, NY, USA, in 2014.

In 2012, he was an Intern with Rambus Inc., Sunnyvale, CA, USA, designing energy-efficient I/O circuits. He is currently the E. E. Landsman (1958) Career Development Assistant Professor with the Department of Electrical Engineering and Computer Science, Massachusetts Institute of Technology, Cambridge, MA, USA. His current research interests include microelectronic circuits and systems operating at millimeter-wave and terahertz frequencies for novel sensing and ultrahigh-speed communications.

Dr. Han is a member of the IEEE Solid-State Circuits Society and the IEEE Microwave Theory and Techniques Society. He was a recipient of the Cornell ECE Director's Ph.D. Thesis Research Award, Cornell ECE Innovation Award, and the Best Student Paper Award (2nd place) of the 2012 Radio-Frequency Integrated Circuits Symposium. He was also a recipient of the Irwin and Joan Jacobs Fellowship, the John M. Olin Fellowship, the IEEE Microwave Theory and Technique Society Graduate Fellowship Award, and the IEEE Solid-State Circuits Society Predoctoral Achievement Award.